

Article

On Thermal Expansion and Density of CGI and SGI Cast Irons

Taishi Matsushita *, Ehsan Ghassemali †, Albano Gómez Saro †, Lennart Elmquist and Anders E. W. Jarfors †

Department of Materials and Manufacturing, School of Engineering, Jönköping University, P.O. Box 1026, Jönköping SE-551 11, Sweden; E-Mails: ehsan.ghassemali@jth.hj.se (E.G.); albanogs@hotmail.com (A.G.S.); lennart.elmquist@jth.hj.se (L.E.); anders.jarfors@jth.hj.se (A.E.W.J.)

† These authors contributed equally to this work.

* Author to whom correspondence should be addressed; E-Mail: taishi.matsushita@jth.hj.se; Tel.: +46-36-101697; Fax: +46-36-166560.

Academic Editor: Hugo F. Lopez

Received: 30 April 2015 / Accepted: 26 May 2015 / Published: 4 June 2015

Abstract: The thermal expansion and density of Compacted Graphite Iron (CGI) and Spheroidal Graphite Iron (SGI) were measured in the temperature range of 25–500 °C using push-rod type dilatometer. The coefficient of the thermal expansion (CTE) of cast iron can be expressed by the following equation: $CTE = 1.38 \times 10^{-5} + 5.38 \times 10^{-8} N - 5.85 \times 10^{-7} G + 1.85 \times 10^{-8} T - 2.41 \times 10^{-6} R_{P/F} - 1.28 \times 10^{-8} NG - 2.97 \times 10^{-7} GR_{P/F} + 4.65 \times 10^{-9} TR_{P/F} + 1.08 \times 10^{-7} G^2 - 4.80 \times 10^{-11} T^2$ (N : Nodularity, G : Area fraction of graphite (%), T : Temperature (°C), $R_{P/F}$: Pearlite/Ferrite ratio in the matrix).

Keywords: thermal expansion; high-silicon cast iron; dilatometer; density; cycle test

1. Introduction

The development and use of high performance powertrain components is crucial for the performance of different vehicles. In order to meet the demands for more efficient transport solutions involving improved energy conversion efficiency in engines as well as lighter components and systems for overall enhanced performance, lighter and/or stronger materials are an important means.

Key materials for engine components (such as engine blocks, cylinder heads, *etc.*) include various cast materials such as cast irons of different grades as well as light metals as aluminum. For heavy truck diesel engines, current and future expected solutions are based on cast irons. For car engines, aluminum is often combined with other metals, as in the case of cast aluminum engine block with cast iron cylinder liners. Legislation and needs for lower emissions and improved efficiency mean higher pressures and temperatures and thus increasing demands on material performance in both cases. Moreover, the downsizing of engines with preserved demands on performance adds to this scenario. To meet these requirements, it is important to investigate factors necessary to create conditions for closer tolerances and optimization of mechanical and thermal properties by control of graphite morphology.

The idea of near net shape is to explore the possibility of designing and casting components with better tolerance and more accurate dimensions to decrease manufacturing cost and required machining. To develop a robust casting process is a prerequisite to cast more accurately. Compacted graphite iron (CGI) has become an interest of the automotive industry [1]. Compacted graphite cast iron is considered more difficult than for grey iron, hence it is interesting to cast with minimal processing requirements. The current project focuses on the casting itself and includes both simulation and verification through field trials.

A possibility to reduce the variations in matrix hardness is to use a material with higher Si content to create a solid solution strengthened ferritic matrix instead [2]. As the solution strengthening effect is achieved by an increased Si-content, this also reduces the carbides as Si is known to reduce tendency for carbide formation in cast irons. For solution strengthened ductile iron a number of interesting properties are obtained, and the existing requirements for mechanical properties fulfilled (similar to a matrix consisting of 50% ferrite and 50% perlite). However, for the same UTS, silicon solution strengthened iron shows higher ductility compared to the one with 50% pearlite. Furthermore, the obtained hardness is uniform and usually falls within ± 5 HBW. The same approach can also be applied to compacted graphite iron material with increased Si content, yielding UTS of 565 MPa, elongation of 10% and hardness of 207 HBW. For CGI materials SinterCast has obtained one patent for solution hardening [3].

For the matrix, both Carbon and Silicon will have solution hardening contributions where size differences and effective change in the shear modulus are direct factors for the effectiveness of the alloying [4]. Elements such as silicon and carbon are also strongly coupled thermodynamically adding to the difficulty of finding an optimum. This also results because there is a strong influence from other elements such as Vanadium [5].

The research focus will be on how the additions of elements responsible for solution hardening affect nucleation and growth and to what extent nucleation is affected by venturing outside the conventional concentration range for CGI materials. For graphite morphology, Sulfur and Oxygen influence nodularity as does Magnesium [6]. Similarly solidification rate too has a significant effect.

Therefore, the current project is focused on Si-alloyed compacted graphite iron, to enable use of Si-alloyed CGI with potentially more robust manufacturing and better casting properties for engines components. Interaction of Si within CGI material is very complex and not fully understood. Some studies suggest that Si-alloyed compacted graphite iron does not meet the requirements imposed on the material. Among other things, lower thermal conductivity has been highlighted and excessive Si content can affect the machinability [7]. The conclusion is that more research is needed to clarify

the Si-alloyed CGI capability, involving casting of samples and examination of mechanical properties, machinability and thermal conductivity.

The current work addresses the aspect of thermal properties and mechanical behavior. As temperature in engine applications requires both the understanding of thermal expansion and the effect of thermal cycling on thermal expansion both aspects are currently addressed for both ferritic-perlitic materials and for fully ferritic materials with different graphite morphology.

2. Experimental

2.1. Materials

The chemical compositions of different cast iron supplied in the present study are given in Table 1.

Table 1. Chemical compositions of the different cast iron (mass %).

Elements	SGI-1	SGI-2	SGI-3	CGI-1	CGI-2
C	3.28	3.13	3.51	3.24	3.18
Si	3.73	4.25	2.36	3.44	3.87
Mn	0.169	0.169	0.408	0.17	0.167
P	0.009	0.0095	0.0063	0.0069	0.0072
S	0.0056	0.0065	0.0043	0.0062	0.0072
Cr	0.028	0.029	0.025	0.028	0.028
Ni	0.045	0.041	0.039	0.048	0.047
Mo	0.0012	0.0016	0.0028	0.0034	0.0037
Mg	0.037	0.036	0.036	0.0061	0.0062
Fe	Balance	Balance	Balance	Balance	Balance
CE ¹	4.53	4.55	4.30	4.39	4.47

¹ CE: Carbon Equivalent = $C\% + (Si\% + P\%)/3$.

The samples for the thermal expansion measurement were taken from a cast component shown in Figure 1, from different thickness (t). In the present study, the samples from following plates were used: SGI-1 ($t = 50$ mm); SGI-2 ($t = 15, 50$ and 75 mm); SGI-3 ($t = 15, 50$ and 75 mm); CGI-1 ($t = 50$ mm); and CGI-2 ($t = 15, 50$ and 75 mm).

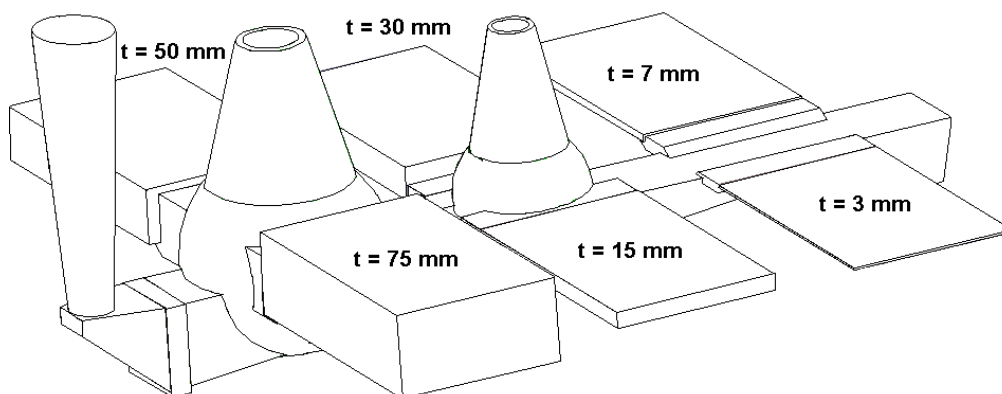


Figure 1. A schematic illustration of the cast component.

The thinner plate is corresponding to the faster cooling rate during the casting and the microstructure will be changed accordingly.

2.2. Dilatometry

Thermal expansion measurements were carried out from room temperature to 500 °C during heating cycle at the rate of 5 K/min using a Netzsch DIL 402 C push-rod dilatometer (Selb, Germany). The experimental apparatus consisted of a heating chamber, a displacement transducer, a digital system for logging (computer) and a push-rod.

The samples subjected for thermal cycling were heated and cooled 46 times between 55 °C and 600 °C with 10 K/min. The heating rate and maximum temperature were slightly changed with single cycle tests due to the limitation of experimental apparatus.

An alumina standard sample (6 mm in diameter × 12 mm in length) was used for the baseline measurement. The cast iron samples were cut into cylindrical pieces (6 mm in diameter × 12 mm in length). The sample was cleaned with acetone before experiments. After the sample was placed in the chamber, the chamber was flushed three times by helium. The temperature was measured with a Type S thermocouple set beside the sample. The temperature and change in length were recorded in the computer. The coefficient of thermal expansion (CTE) was obtained from the slope of $\Delta L/L_{X0}$ (where ΔL : change in length and L_{X0} : initial length) against temperature. The details of the analysis method are described in Appendix A.

2.3. Microstructural Characterization

In many cases, the thermophysical properties of cast irons are influenced by microstructures such as nodularity, graphite amount and pearlite/ferrite ratio. The microstructure of the component will be influenced by the cooling rate during the casting. As mentioned in the Experimental section, the samples were taken from $t = 15, 50$ and 75 mm parts in this study to investigate the influence of the microstructure. The nodularity and graphite amount of each sample were measured using optical microscope Leica Leitz DMRX (Wetzlar, Germany) with Leica Q-Win v3 software (Wetzlar, Germany). The magnification was $100\times$. Minimum length of graphite was set as $10\ \mu\text{m}$ for nodularity measurement. Forty pictures were taken for each sample to cover an area larger than $10\ \text{mm}^2$. The nodularity was measured with the following equation (ISO standard method [8]).

$$\text{Nodularity (\%)} = \frac{\sum A_{\text{Graphite (ISO form VI)}} + 0.5 \sum A_{\text{Graphite (ISO form IV + V)}}}{\sum A_{\text{Graphite (All)}}} \times 100\% \quad (1)$$

where $A_{\text{Graphite (IOS form VI)}}$: the surface area of graphite with roundness higher than 0.625 (ISO 945 form VI); $A_{\text{Graphite (ISO form IV+V)}}$: the surface area of graphite with roundness between 0.525 and 0.625 (ISO 945 form IV and V); and $A_{\text{Graphite (All)}}$: the surface area of all graphite.

3. Results and Discussion

3.1. Microstructure

The measured nodularity, graphite amount and ferrite/perlite amount are summarized in Tables 2 and 3, respectively. The amount of graphite in Table 3 represents the area fraction of graphite.

Table 2. Nodularity (%) of samples.

Thickness (mm)	SGI-1	SGI-2	SGI-3	CGI-1	CGI-2
15	-	30.7	75.4	-	17.0
50	66.4	55.6	74.9	15.7	7.33
75	-	53.7	82.6	-	3.92

Table 3. Graphite and ferrite/perlite area fractions (%).

Samples	Graphite	ASTM Ferrite	ASTM Pearlite
SGI-3, 15 mm	3.40	33.96	62.64
SGI-3, 50 mm	7.84	38.60	53.56
SGI-3, 75 mm	8.80	38.67	52.53
SGI-1, 50 mm	9.05	90.95	0
SGI-2, 15 mm	2.12	97.88	0
SGI-2, 50 mm	6.78	93.22	0
SGI-2, 75 mm	5.57	94.43	0
CGI-1, 50 mm	6.09	93.91	0
CGI-2, 15 mm	2.13	97.87	0
CGI-2, 50 mm	2.15	97.85	0
CGI-2, 75 mm	1.94	98.06	0

Some typical microstructures of SGI-3 are shown in Figure 2 (thickness: 15 mm), Figure 3 (thickness: 50 mm) and Figure 4 (thickness: 75 mm). As can be seen from these figures, the graphite size tends to become smaller with decreasing plate thickness due to the faster cooling rate, *viz.*, shorter time for graphite growth. The same trend was found for the SGI-2 as well.

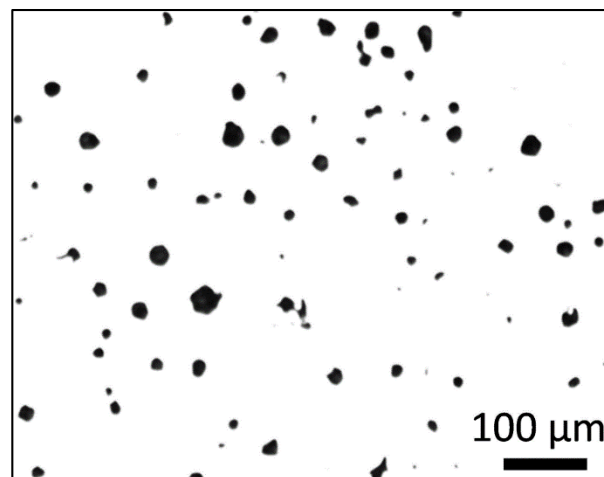


Figure 2. Optical micrograph of the SGI-3 specimen; thickness: 15 mm.

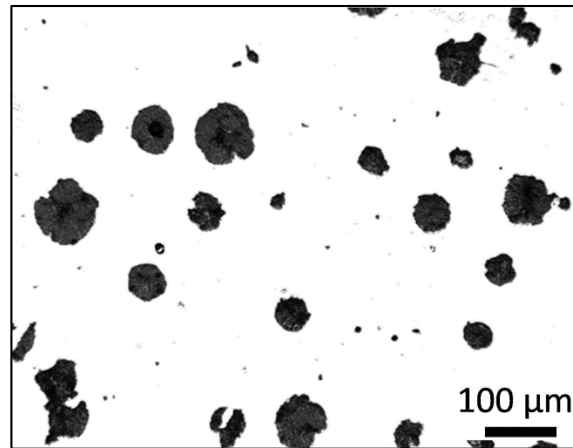


Figure 3. Optical micrograph of the SGI-3 specimen; thickness: 50 mm.

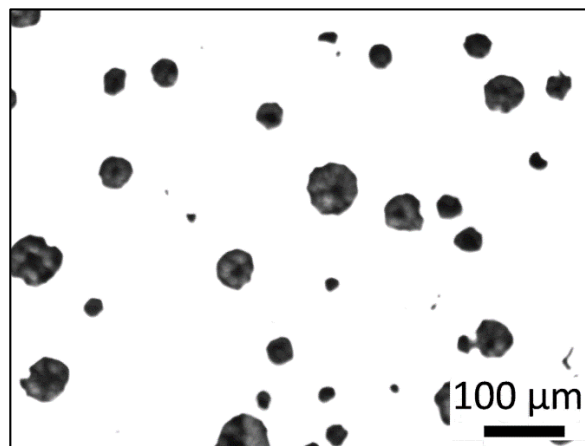


Figure 4. Optical micrograph of the SGI-3 specimen; thickness: 75 mm.

The SGI-3 sample has a fully developed bull's eye structure (Figure 5) and it was confirmed that all other materials in the current study was fully ferritic, Figures 6 and 7.

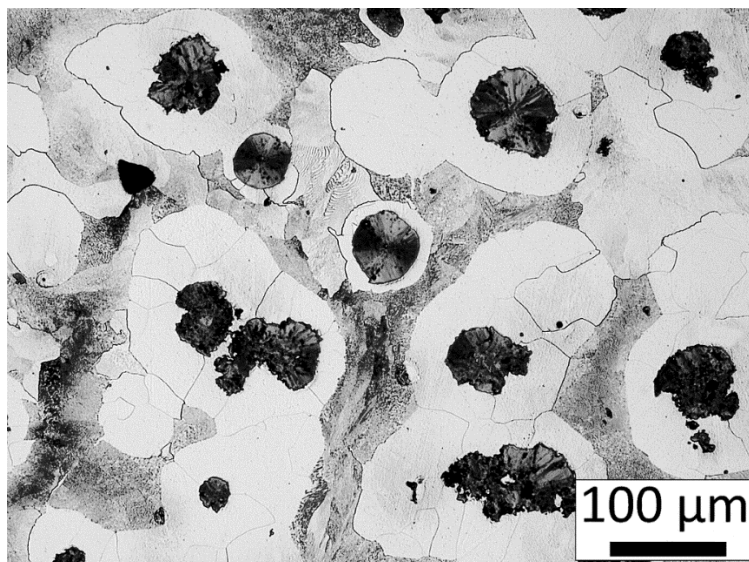


Figure 5. Optical micrograph of the SGI-3 specimen; thickness: 50 mm (Bull's eye).

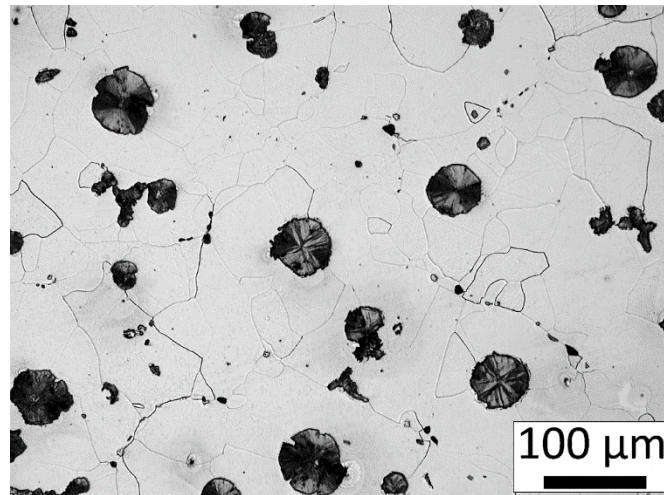


Figure 6. Optical micrograph of the SGI-1 specimen; thickness: 50 mm (Fully ferritic).

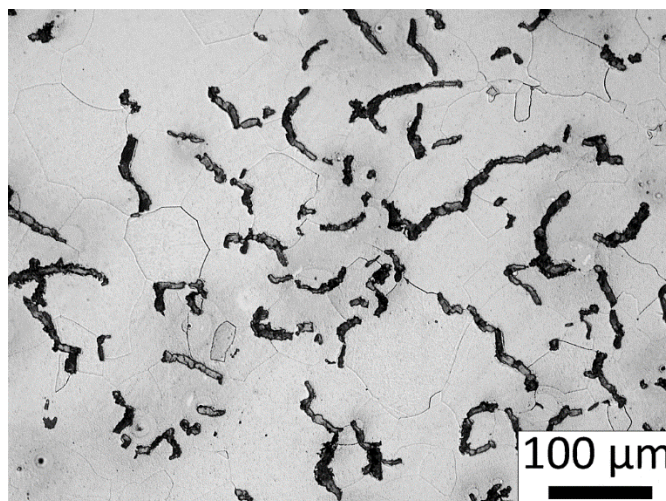


Figure 7. Optical micrograph of the CGI-2 specimen; thickness: 75 mm (Fully ferritic).

3.2. Coefficient of Thermal Expansion (CTE)

Figures 8–10 show the CTE of sample SGI-2, SGI-3 and CGI-2, respectively.

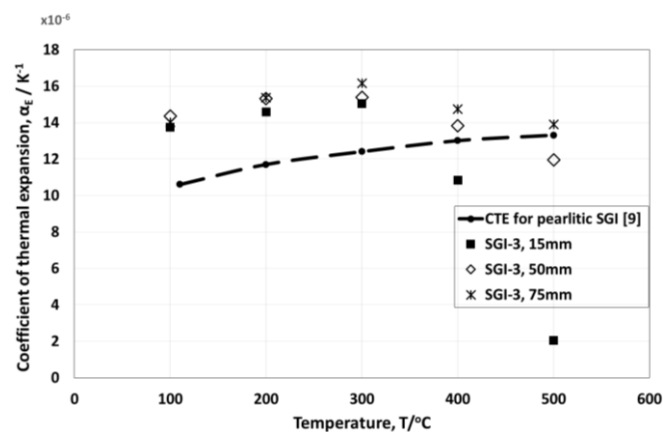


Figure 8. Coefficient of thermal expansion (CTE) of SGI-3 (15, 50 and 75 mm) as a function of temperature (during heating cycles).

As can be seen in Figure 8, the CTE tends to increase with increasing ferrite amounts in the matrix (ferrite amount: SGI-3, 15 mm = 34%, SGI-3, 50 mm and 75 mm = 39%) and the trend agrees with the literature data [9].

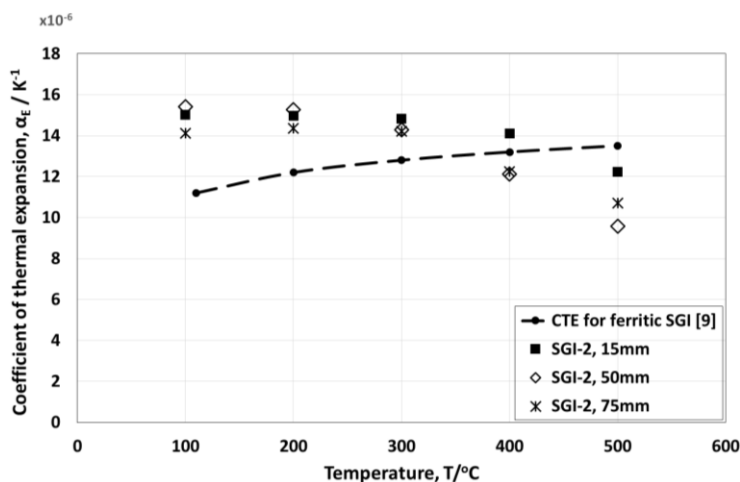


Figure 9. CTE of SGI-2 (15, 50 and 75 mm) as a function of temperature (during heating cycles).

The SGI-2 samples are fully ferritic. In this case, the results can be explained by the graphite amount in the microstructure. As shown in Table 3, the graphite amount in SGI-2, 15, 50 and 75 mm, are 2.12%, 6.78% and 5.57%, respectively, and the CTE is decreasing with increasing graphite (which has much lower CTE than matrix) amounts (Figure 9). The matrices of SGI-2 samples are 100% ferritic. Therefore, there is no influence of the ferrite/pearlite ratio and graphite amount is a dominant factor.

On the other hand, in the case of ferrite/pearlite matrix (SGI-3 in Figure 8), the samples that have higher graphite amounts (SGI-3, 50 mm and 75 mm) show higher CTE. This opposite trend indicates that the ferrite/pearlite ratio plays a more important role than graphite amount.

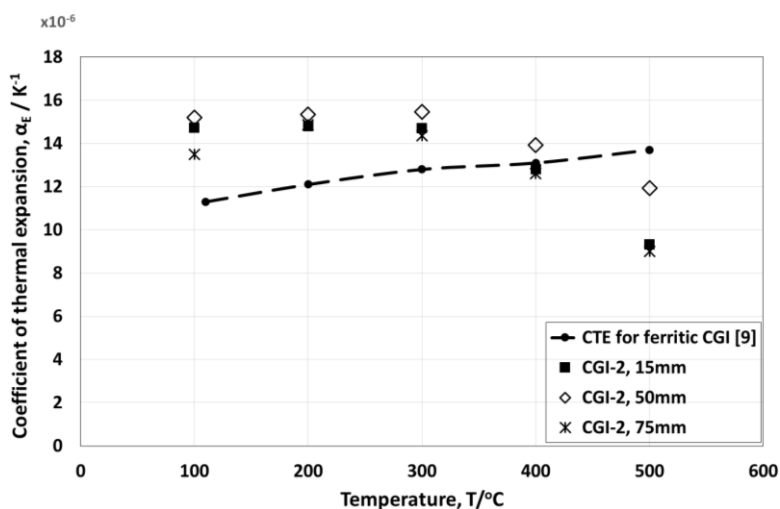


Figure 10. CTE of CGI-2 (15, 50 and 75 mm), as a function of temperature (during heating cycles).

The graphite amount in CGI-2, 15, 50 and 75 mm, are almost the same (about 2%) and it seems there is no relation between nodularity and CTE (Figure 10). The CTE of the SGI and CGI cast irons are summarized in Figure 11.

For the samples that have fully ferritic matrix and higher graphite (which has a much lower CTE than matrix) amounts tend to show the lower CTE.

The SGI-3 (which has lowest ferrite in matrix) shows the higher CTE. In the previous section, it has been concluded that the ferrite/pearlite ratio are playing a more important role than the graphite amount (Figures 8 and 9). The result in Figure 11 is in contradiction with this explanation. The sample composition in Figure 11 is not same and it might not be comparable.

According to the literature [9], CTE of SGI is higher than that of Grey cast iron and CTE of CGI is between SGI and Grey cast iron. However, in our results, the CGI tends to show the higher CTE.

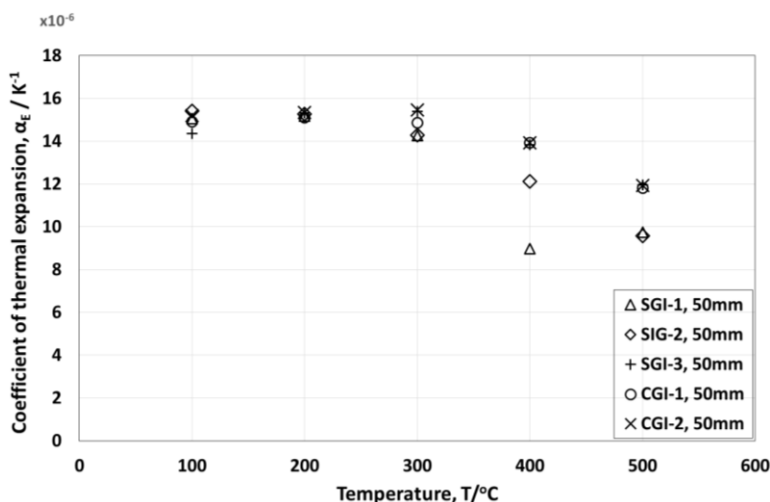


Figure 11. CTE of SGI-1, SGI-2, and SGI-3 (50 mm) and CGI-1 and CGI-2 (50 mm) as a function of temperature (during heating cycles).

Extensive studies have been made to find the influence of microstructure on the CTEs based on the present experimental results. It has been tried to obtain empirical equation to express the CTE using experimental results as a function of nodularity, amount of graphite, temperature and Pearlite/Ferrite ratio in the matrix. The CTE can be expressed by the following equation.

$$CTE = 1.38 \times 10^{-5} + 5.38 \times 10^{-8} N - 5.85 \times 10^{-7} G + 1.85 \times 10^{-8} T - 2.41 \times 10^{-6} R_{P/F} - 1.28 \times 10^{-8} NG - 2.97 \times 10^{-7} GR_{P/F} + 4.65 \times 10^{-9} TR_{P/F} + 1.08 \times 10^{-7} G^2 - 4.80 \times 10^{-11} T^2 \quad (2)$$

where *N*: Nodularity; *G*: Area fraction of graphite (%); *T*: Temperature (°C); and *R_{P/F}*: Pearlite/Ferrite ratio in the matrix.

The Cook’s distance [10], which show how much the regression changes if a data point is deleted, was calculated to obtain a statically reliable equation and three outliers were ignored to derive the above equation. The *R*² value of the above equation is 0.87. As can be seen in Equation (1), the influence of the following terms on the CTE is negligible: *GT*, *NR_{P/F}*, *TN*, *N*² and *R*²_{P/F}.

3.3. Density

The density was calculated using the results of dilatometer experiments for each material. It is assumed that the materials are isotropic and volumetric CTE, *α_v*, is three times of linear CTE, *α_E*.

$$\alpha_v = 3\alpha_E \quad (3)$$

The density at room temperature was measured by Archimedes’ method and the results are shown in Table 4.

Table 4. Density at room temperature ($\text{g}\cdot\text{cm}^{-3}$).

Thickness	SGI-1	SGI-2	SGI-3	CGI-1	CGI-2
15 mm	-	7.04	7.11	-	7.06
50 mm	7.02	7.04	7.10	7.04	7.04
75 mm	-	7.04	7.10	-	7.05

The density changes during the heating process are shown in Figures 12 and 13.

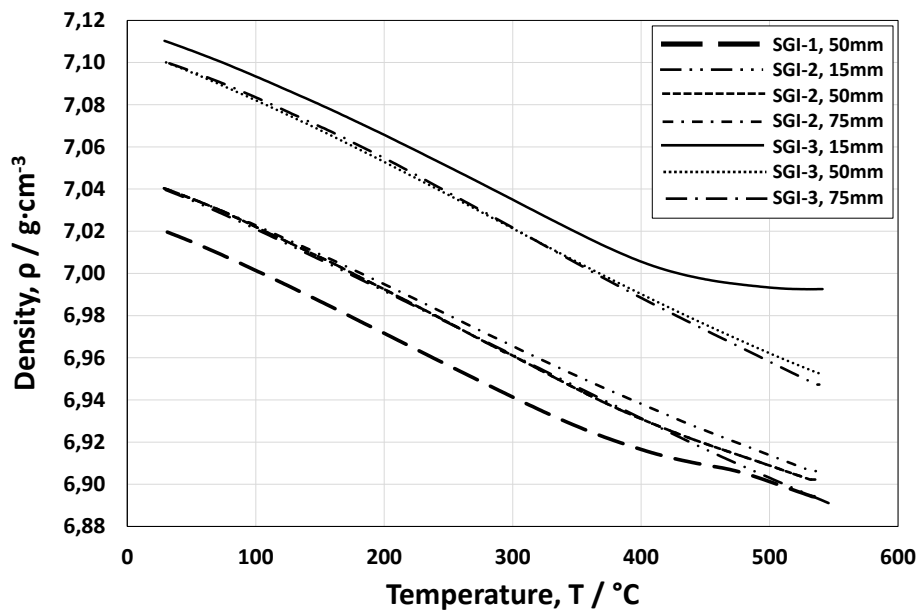


Figure 12. Density of the SGI as a function of temperature (during heating cycle).

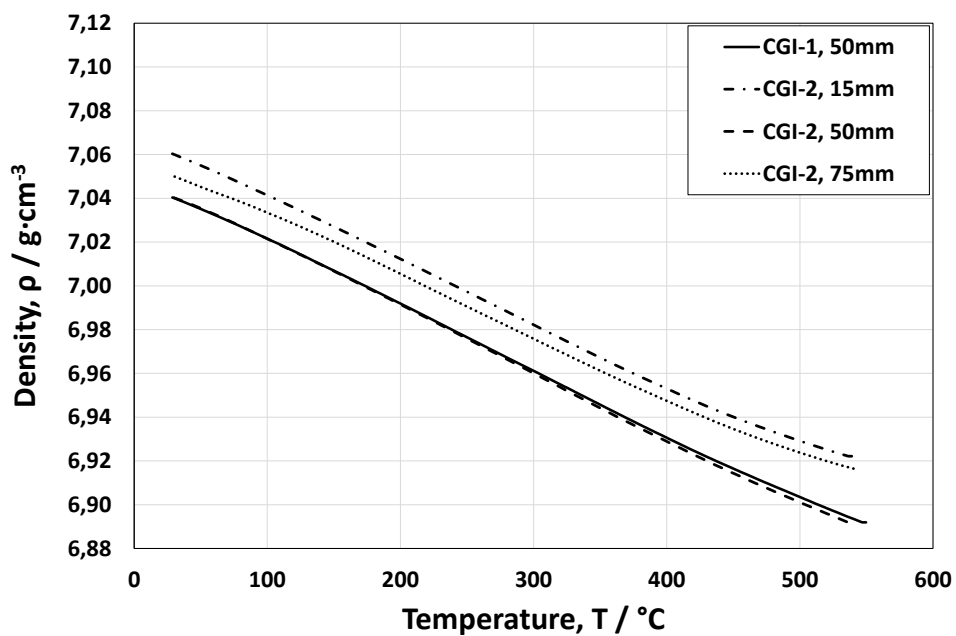


Figure 13. Density of the CGI as a function of temperature (during heating cycle).

3.4. Effect of Thermal Cycling on Thermal Expansion

The dL/L_0 values at 55 °C are plotted against the number of cycles and shown in Figures 14 and 15.

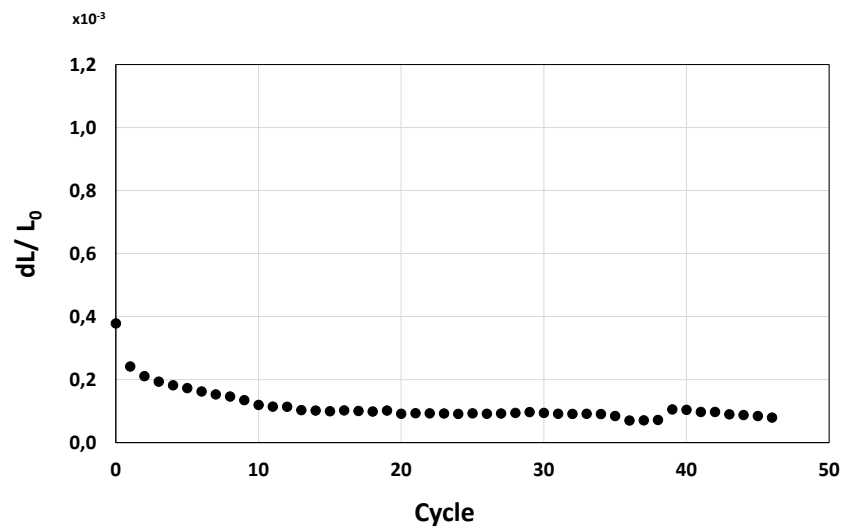


Figure 14. Thermal expansion behavior of the SGI-1 (thickness: 30 mm) during thermal cycling (dL/L_0 at 55 °C).

As shown in Figure 14, for the SGI-1, the dL/L_0 at 55 °C was decreased from the beginning and became constant. The SGI-1 has a ferritic matrix, as shown in Figure 6. However, the decomposition of retained cementite into graphite and ferrite might occur in the vicinity of the maximum temperature in the measurement (600 °C), since the samples contains relatively high silicon. Usually, the volume is increased by the graphitizing. However, in the present case, the vacancy or pores of already existing graphite phase seem to be filled with the decomposed carbon and the influence of the filling of the pore with carbon is superior to the volume expansion due to the graphitizing. As a result, the total volume seems to become smaller. The volume change seems to occur by the competition of these two effects.

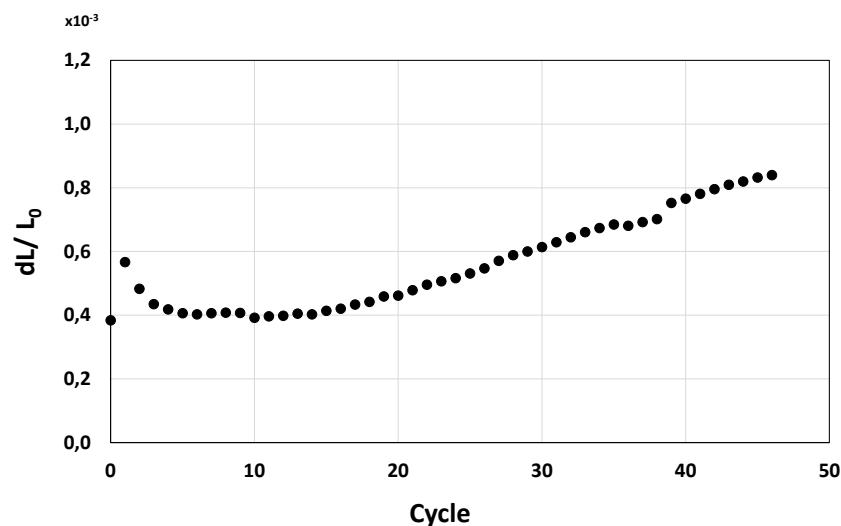


Figure 15. Thermal expansion behavior of the SGI-3 (thickness: 30 mm) during thermal cycling (dL/L_0 at 55 °C).

For the SGI-3, the volume was increased in the first cycle. In this case, the increasing of volume due to the graphitizing might be superior to the shrinkage by the filling effect and the total volume seems to be increased in the first cycle. In the cycle test, the volume of the SGI-3 is increased in the first cycle. However, in the single cycle experiment, the volume of the SGI-3 is decreased from beginning as SGI-1. It implies that the trend of volume change depends on the amount of pore or vacancy in the graphite phase. In the cycle test, the volume starts to decrease from the second cycle and after the incubation time, that is, the stage where the increasing of the volume due to the local graphitization and the decreasing of the volume due to the filling effect is balanced, the volume is increased again. The volume is increased constantly after 15 cycles. This might be an influence of constant change of phases and microstructure, that is, the phase and microstructure are approaching to the steady state under the present experimental condition and continuous decomposition of cementite. The SEM images of SGI-3 before and after the cycle tests are shown in Figure 16. The SGI-3 has bull's eye structure as shown in Figure 5. However, some graphite ais surrounded by pearlite as, shown in Figure 16, and the bridges of cementite were observed between the graphite and matrix. These bridges might be acting as a bypass for the carbon diffusion. As can be seen in Figure 16b, it was observed that the cementite bridges on the graphite side is graphitized after the cycle tests. The volume seems to be expanded due to the local graphitization. In addition, the binding between the original graphite phase and matrix might become loose and the gap might become larger due to the graphitizing of the cementite bridge. Figure 17 shows this phenomenon in more details.

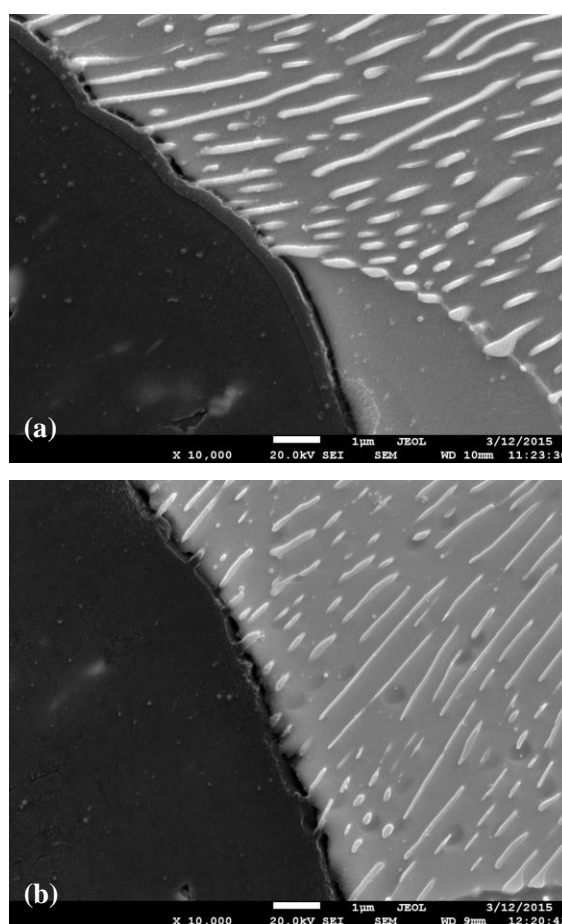


Figure 16. SEM images of SGI-3 (a) before and (b) after thermal cycling tests.

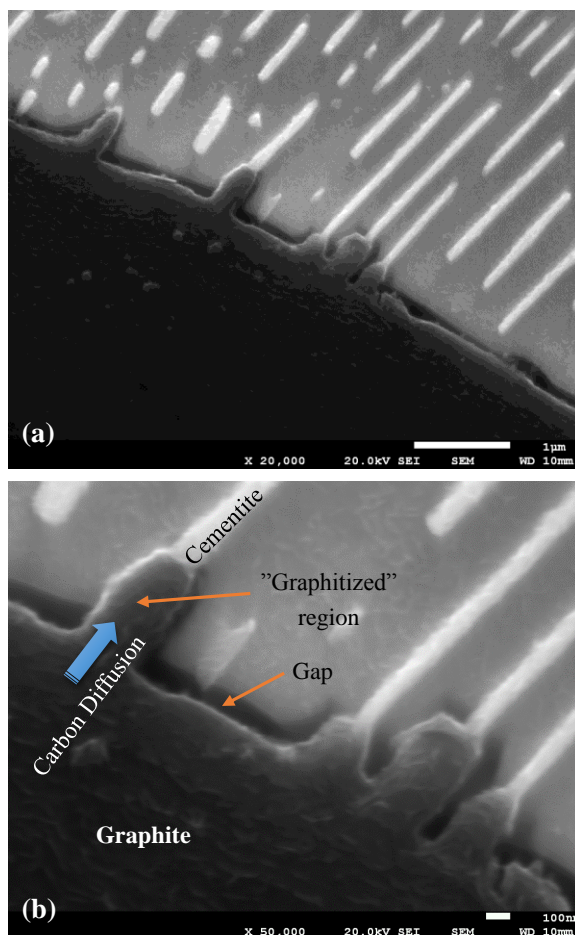


Figure 17. SEM images of SGI-3 showing local graphitization after cycling test, in two different magnifications: (a) low magnification and (b) high magnification.

For the qualitative justification, more investigation on the relative atomic volume change of Fe₃C and graphite is required.

3.5. Uncertainty of Measurements

The experimental results were assessed based on Guide to the expression of Uncertainty in Measurement (GUM) [11,12]. The values of each factor are summarized in the Appendix A.

3.5.1. Uncertainty of α_{RS}

The CTE of reference material is $8.00 \times 10^{-6} \pm 0.1 \times 10^{-6} \text{ K}^{-1}$ at 300 °C. Hence the uncertainty of the α_{RS} can be described by the following equation.

$$u(\alpha_{RS}) = \sqrt{\int_{m-a}^{m+a} \frac{1}{2a} (x-m)^2 dx} = \frac{a}{\sqrt{3}} = \frac{0.1 \times 10^{-6}}{\sqrt{3}} = 5.8 \times 10^{-8} (\text{K}^{-1}) \tag{4}$$

where *m* is the standard value and *a* is the tolerance.

3.5.2. Uncertainty of δα_{RS}

The uncertainty of δα_{RS} can be assessed as follows.

$$u(\delta\alpha_{RS}) = u(q \times \Delta T) \quad (5)$$

where q is the slope of α_{RS} against temperature, which is obtained by least-square method. In the present paper, the standard α_{RS} values at 275, 300 and 325 °C were used to obtain the slope. The uncertainty of q depends on the uncertainty of α_{RS} and it can be described as follows.

$$u(q) = \frac{u(\alpha_{RS})}{\sqrt{\sum (T_k - \bar{T})^2}} = \frac{5.8 \times 10^{-8}}{35} = 1.7 \times 10^{-9} (\text{K}^{-2}) \quad (6)$$

where \bar{T} is the average of the three temperatures, viz., 300 °C.

Hence the uncertainty of $\delta\alpha_{RS}$ at 300 °C is

$$u(\delta\alpha_{RS}) = 1.7 \times 10^{-9} \times 20 = 3.4 \times 10^{-8} (\text{K}^{-1}) \quad (7)$$

3.5.3. Uncertainty of δT

The uncertainty of the δT can be estimated from the sample deformation during the measurement.

The tolerance of the melting point due to the impurity of the sample was assumed ± 0.5 °C.

The uncertainty of the reading of values were assumed to be 0.2 °C (standard deviation).

The resolution of the temperature measurement is 0.1 °C, viz., tolerance is ± 0.05 °C.

The δT will be changed by the sample position and thermal property of the sample and the reproducibility of the measurement is assumed to be 0.5 °C (standard deviation) in the present measurement.

Hence the uncertainty of the δT at melting point can be described as follows:

$$u(\delta T_{\text{mp}}) = \sqrt{\left(\frac{0.5}{\sqrt{3}}\right)^2 + (0.2)^2 + \left(\frac{0.05}{\sqrt{3}}\right)^2 + (0.5)^2} = 0.61 (\text{K}) \quad (8)$$

The δT at 300 °C can be obtained from the melting points of Tin ($T_{\text{mp,Sn}} = 231.9$ °C) and Lead ($T_{\text{mp,Zn}} = 327.5$ °C) by the Linear interpolation.

$$\delta T = \frac{300 - T_{\text{mp,Sn}}}{T_{\text{mp,Zn}} - T_{\text{mp,Sn}}} (\delta T_{\text{Zn}} - \delta T_{\text{Sn}}) + \delta T_{\text{Sn}} \quad (9)$$

Furthermore, it may be arranged as follows:

$$\delta T = (\delta T_{\text{Zn}} - \delta T_{\text{Sn}}) \cdot \frac{T - (T_{\text{mp,Sn}} + T_{\text{mp,Zn}}) / 2}{T_{\text{mp,Zn}} - T_{\text{mp,Sn}}} + (\delta T_{\text{Zn}} + \delta T_{\text{Sn}}) \cdot \frac{1}{2} \quad (10)$$

Hence, the uncertainty of δT at 300 °C is

$$u(\delta T) = \sqrt{2 \times \left(\frac{300 - \frac{T_{\text{mp,Sn}} + T_{\text{mp,Zn}}}{2}}{T_{\text{mp,Zn}} - T_{\text{mp,Sn}}} \right)^2 + 2 \times \left(\frac{1}{2}\right)^2 \times u(\delta T_{\text{mp}})} \approx 0.47 (\text{K}) \quad (11)$$

3.5.4. Uncertainty of δT^*

$$\begin{aligned}
 u(\delta T^*) &= \frac{\Delta T}{T_{\text{mp,Zn}} - T_{\text{mp,Sn}}} \cdot \sqrt{u^2(\delta T_{\text{mp,Sn}}) + u^2(\delta T_{\text{mp,Zn}})} \\
 &= \frac{20}{327.5 - 231.9} \cdot \sqrt{(0.21)^2 + (0.21)^2} = 0.062(\text{K})
 \end{aligned}
 \tag{12}$$

3.5.5. Uncertainties of $\Delta L_{\text{RS}}^m(T)$ and $\Delta L_X^m(T)$

The uncertainties of $\Delta L_{\text{RS}}^m(T)$ and $\Delta L_X^m(T)$ depend on the resolution of the displacement transducer. The resolution of transducer is 1.25 nm and the ΔL was derived from the measurement at two different temperatures, viz., at $T \pm \Delta T/2$. Hence the uncertainties of $\Delta L_{\text{RS}}^m(T)$ and $\Delta L_X^m(T)$ are

$$u(\Delta L^m(T)) = \sqrt{\left(\frac{\left(\left(\frac{1.25}{2} \right) \times 10^{-9} \right)^2}{\sqrt{3}} \right)^2} \times 2 = 5.1 \times 10^{-10} (\text{m})
 \tag{13}$$

3.5.6. Uncertainties of $L_{\text{RS}0}$ and L_{X0}

The length of the specimens was measured using a micrometer, which has 0.001 mm resolution and ± 0.002 mm nominal accuracy.

The deviation of the temperature from 20 °C is assumed ± 5 °C.

$$\begin{aligned}
 u(L_0) &= \sqrt{u^2(\sigma_{\text{mic}}) + u^2(R_{\text{mic}}) + u^2(\Delta T_D)} = \sqrt{\left(\frac{\sigma_{\text{mic}}}{\sqrt{3}} \right)^2 + \left(\frac{R_{\text{mic}}}{\sqrt{3}} \right)^2 + \left(\alpha(20 \text{ °C}) \times L_0 \times \frac{\Delta T_{20}}{\sqrt{3}} \right)^2} \\
 &= \sqrt{\left(\frac{2 \times 10^{-6}}{\sqrt{3}} \right)^2 + \left(\frac{1 \times 10^{-6}}{\sqrt{3}} \right)^2 + \left(\alpha_{\text{RS}}(20 \text{ °C}) \times 12 \times 10^{-3} \times \frac{5}{\sqrt{3}} \right)^2}
 \end{aligned}
 \tag{14}$$

where σ_{mic} is the nominal accuracy of the micrometer and R_{mic} is the resolution of the micrometer. As can be seen from the above equation, the CTE at 20 °C, $\alpha(20 \text{ °C})$, is required. However, the order of CTE of alumina and cast iron are 10^{-6} and 10^{-5} , respectively. Hence, the third term in the above equation is negligible. Therefore the uncertainties of $L_{\text{RS}0}$ and L_{X0} , $u(L_0)$, is

$$u(L_0) \approx 1.19 \times 10^{-6} (\text{m})
 \tag{15}$$

3.5.7. Combined Standard Uncertainty

The combined standard uncertainty, $u_c(\alpha_x)$ can be described by the following equation.

$$u_c^2(\alpha_x) = \sum \left(\frac{\partial f}{\partial x_i} \right)^2 \cdot u^2(x_i)
 \tag{16}$$

where $\alpha_x (=f(x_i))$ is the CTE of the sample; x_i is the factor of each uncertainty.

As an example, a combined standard uncertainty of the measurement result of SGI-3, 50 mm at 300 °C ($\alpha_x = 1.54 \times 10^{-5}$, $\alpha_x^m = 7.82 \times 10^{-6}$, $\Delta L_x^m = 1.88 \times 10^{-6}$) was evaluated and following value was obtained.

$$u_c(\alpha_x) = 6.39 \times 10^{-8} \text{ (1/K)} \quad (17)$$

4. Conclusions

The CTE and density of SGI and CGI materials were measured as a function of temperature in the temperature range of room temperature to 500 °C (600 °C for the cycle tests).

Based on the microstructure characterization, empirical equations for the CTE were derived and it can be described by the following equation:

$$\begin{aligned} \text{CTE} = & 1.38 \times 10^{-5} + 5.38 \times 10^{-8} N - 5.85 \times 10^{-7} G + 1.85 \times 10^{-8} T - 2.41 \times 10^{-6} R_{P/F} \\ & - 1.28 \times 10^{-8} NG - 2.97 \times 10^{-7} GR_{P/F} + 4.65 \times 10^{-9} R_{P/F} + 1.08 \times 10^{-7} G^2 - 4.80 \times 10^{-11} T^2 \end{aligned} \quad (2)$$

N : Nodularity; G : Area fraction of graphite (%); T : Temperature (°C); and $R_{P/F}$: Pearlite/Ferrite ratio in the matrix.

The expansion and shrinkage at a constant temperature in the cycle tests could be explained by the volume change due to the local graphitization.

The uncertainty of the CTE measurement was assessed using the GUM method and it was assessed that the combined standard uncertainty of the CTE is 6.39×10^{-8} (1/K) under a specific condition.

Acknowledgments

The authors thank the Knowledge Foundation, CompCast project for their financial supports.

Author Contributions

T.M., E.G. and A.G.S. performed the experiments; T.M. analyzed the data; T.M., E.G. and A.E.W.J. wrote the paper; A.E.W.J. supervised the work; L.E. contributed materials.

Appendix A: Analysis of CTE

The measured sample length at temperature T , $L_A^m(T)$, which is detected by the displacement transducer can be described by Equation (18).

$$L_A^m(T) = L_A(T + \delta T_A) + L_{PR}(T) - L_{SC}(T) \quad (18)$$

where T is the temperature measured by the thermocouple; $L_A(T + \delta T_A)$ is the length of the sample at sample temperature $T + \delta T_A$; δT_A is the temperature difference between the temperature measured by the thermocouple and the temperature of the sample; $L_{PR}(T)$ is the length of the push rod; and $L_{SC}(T)$ is the length of the sample carrier.

The term $L_A(T + \delta T_A)$, in the above equation can be expressed by using the CTE as follows.

$$L_A(T + \delta T_A) = L_A(T) + L_{A0}\alpha_A(T)\delta T_A + \frac{1}{2}L_{A0}\frac{\delta\alpha_A}{\Delta T}(\delta T_A)^2 \quad (19)$$

where $L_A(T)$ is the length of the sample at sample temperature T ; L_{A0} is the length of the sample at room temperature; $\alpha_A(T)$ is the CTE at temperature T ; and $\delta\alpha_A$ is the change of the CTE due to the temperature change, ΔT , in the vicinity of temperature T .

From Equations (18) and (19), the L_A^m at temperature $T + \Delta T/2$ and $T - \Delta T/2$ can be calculated and the measured CTE at temperature T can be described as follows [10].

$$\begin{aligned}\alpha_A^m(T) &\equiv \frac{L_A^m(T + \Delta T/2) - L_A^m(T - \Delta T/2)}{\Delta T \cdot L_0} \\ &= \alpha_A(T) + \alpha_A(T) \cdot \frac{\delta T_A^*}{\Delta T} + \delta\alpha_A \cdot \frac{\delta T_A}{\Delta T} \cdot \frac{\delta T_A^*}{\Delta T} + \frac{L_{PR}(T) - L_{SC}(T)}{\Delta T \cdot L_0}\end{aligned}\quad (20)$$

where L_0 is the length of the sample; δT_A^* is the change of δT_A corresponding to the change of temperature T (ΔT).

The $\alpha_A^m(T)$ was measured for the alumina (reference) and our samples in the present study. From these values, the term $\frac{L_{PR}(T) - L_{SC}(T)}{\Delta T \cdot L_{S0}}$ in the above equation can be cancelled and the CTE of the sample at temperature T , $\alpha_X(T)$, can be described as follows.

$$\alpha_X(T) = \alpha_{RS}(T) + \frac{\Delta T}{\Delta T + \delta T^*} \left(\alpha_X^m(T) - \alpha_{RS}^m(T) \right) - (\delta\alpha_X - \delta\alpha_{RS}) \cdot \frac{\delta T \cdot \delta T^*}{\Delta T \cdot (\Delta T + \delta T^*)}\quad (21)$$

where $\alpha_{RS}(T)$ is the CTE of the alumina (reference) at temperature T ; $\alpha_X^m(T) \cdot \left(\equiv \frac{\Delta L_X^m(T)}{\Delta T \cdot L_{X0}} \right)$ is the measured CTE of the sample at temperature T . $\alpha_{RS}^m(T) \cdot \left(\equiv \frac{\Delta L_{RS}^m(T)}{\Delta T \cdot L_{RS0}} \right)$ is the measured CTE of the alumina (reference) at temperature T .

In the present analysis, influence of the sensitivity of the transducer, room temperature change and material dependency of the δT_A due to the difference of the thermal conductivity and endo/exothermic reactions were ignored for the sake of simplicity.

The values used to calculate the CTE of the sample at temperature T , $\alpha_X(T)$, are summarized in Table 5.

The value of α_{RS} and $\delta\alpha_{RS}$ was taken from the Netzsch's standard [13] for the temperature range from 25 °C to 550 °C.

Table 5. Input values for the calculation of CTEs.

Parameters	Values
α_{RS}	7.78×10^{-6} (1/K) 100 °C: 3.60×10^{-8} (1/K) 200 °C: 1.76×10^{-7} (1/K)
$\delta\alpha_{RS}$	300 °C: 2.00×10^{-8} (1/K) 400 °C: -2.00×10^{-8} (1/K) 500 °C: 2.00×10^{-8} (1/K)
δT	1 (K)
δT^*	0.01 (K)
$\Delta L_{RS}^m(T)$	Measured value at each temperature range
$\Delta L_X^m(T)$	Measured value at each temperature range
L_{RS0}	1.2×10^{-2} (m)
L_{X0}	1.2×10^{-2} (m)
$\delta\alpha_X$	0 (1/K)
ΔT	20 (K)

Appendix B: List of Symbols

$A_{\text{Graphite (IOS form VI)}}$: Surface area of graphite with roundness higher than 0.625 (ISO 945 form VI);

$A_{\text{Graphite (IOS form IV+V)}}$: Surface area of graphite with roundness between 0.525 and 0.625 (ISO 945 form IV and V);

$A_{\text{Graphite (All)}}$: Surface area of all graphite;

α : tolerance;

CGI: Compacted Graphite Iron;

CTE: Coefficient of thermal expansion;

dL : Change in length;

G : Area fraction of graphite (%);

L_0 : Initial length;

$L_A(T)$: Length of the sample at temperature T ;

$L_A^m(T)$: Measured sample length at temperature T ;

$L_{PR}(T)$: Length of the push rod at temperature T ;

L_{RS0} : initial length of reference sample;

$L_{SC}(T)$: Length of the sample carrier at temperature T ;

L_{X0} : Initial length of sample X ;

m : Standard value;

N : Nodularity;

q : Slope of α_{RS} against temperature;

R_{mic} : Resolution of the micrometer;

$R_{P/F}$: Pearlite/Ferrite ratio in the matrix;

SGI: Spheroidal Graphite Iron;

T : Temperature of the sample;

\bar{T} : Average temperature;

T_k : Selected temperatures to calculate the CTE;

t : Thickness of the component;

$u(x)$: Uncertainty of $x\alpha_A(T)$: CTE of sample A at temperature T ;

α_E : Coefficient of thermal expansion (CTE);

α_{RS} : CTE of alumina (reference);

$\alpha_{RS}(T)$: CTE of the alumina (reference) at temperature T ;

$\alpha_{RS}^m(T) \cdot \left(\equiv \frac{\Delta L_{RS}^m(T)}{\Delta T \cdot L_{RS0}} \right)$: Measured CTE of the alumina (reference) at temperature;

α_V : Volumetric CTE;

α_X : CTE of sample x ;

$\alpha_X^m(T) \cdot \left(\equiv \frac{\Delta L_X^m(T)}{\Delta T \cdot L_{X0}} \right)$: Measured CTE of the sample at temperature T ;

ΔL : Change in length;

$\Delta L_{RS}^m(T)$: Measured ΔL value of reference sample at each temperature range;

$\Delta L_X^m(T)$: Measured ΔL value of sample X at each temperature range;

ΔT : Change of temperature;

ΔT_D : Deviation of the temperature during the L_0 measurement;

$\delta\alpha_{RS}$: Change of the CTE of the alumina (reference) due to the temperature change, ΔT , in the vicinity of temperature T ;

$\delta\alpha_X$: Change of the CTE of the sample X due to the temperature change, ΔT , in the vicinity of temperature T ;

δT : Temperature difference between the temperature measured by the thermocouple and the temperature of the sample;

δT^* : Change of δT corresponding to the change of temperature $T(\Delta T)$;

δT_A : Temperature difference between the temperature measured by the thermocouple and the temperature of the sample A;

δT_A^* : Change of δT_A corresponding to the change of temperature $T(\Delta T)$ for sample A;

δT_{mp} : δT at melting point;

ρ : Density;

σ_{mic} : Nominal accuracy of the micrometer.

Conflicts of Interest

The authors declare no conflict of interest.

References

1. Dawson, S. Compacted Graphite Iron—A Material Solution for Modern Diesel Engine Cylinder Blocks and Heads. *China Foundry* **2009**, *6*, 241–246.

2. Larker, R. In *Solution Strengthened Ferritic Ductile Iron Iso 1083/js/500-10 Provides Superior Consistent Properties in Hydraulic Rotators*, In Proceedings of Keith Millis Symposium on Ductile Iron, Las Vegas, NV, USA, 2008; Hilton Head: South California, CA, USA, pp. 169–177.
3. Hollinger, I. Compacted Graphite Cast Iron Alloy. Swedish Patent 9802418-5, 1998.
4. Sieurin, H.; Zander, J.; Sandström, R. Modelling Solid Solution Hardening in Stainless Steels. *Mater. Sci. Eng.* **2006**, *415*, 66–71.
5. Fras, E.; Kawalec, M.; Lopez, H.F. Solidification Microstructures and Mechanical Properties of High-Vanadium Fe–C–V and Fe–C–V–Si Alloys. *Mater. Sci. Eng.* **2009**, *524*, 193–203.
6. Mampaey, F.; Habets, D.; Plessers, J.; Seutens, F. On Line Oxygen Activity Measurements to Determine Optimal Graphite form during Compacted Graphite Iron Production. *Int. J. Metalcasting* **2010**, *4*, 25–43.
7. Selin, M.; König, M. Regression Analysis of Thermal Conductivity based on Measurements of Compacted Graphite Irons. *Metall. Mater. Trans.* **2009**, *40*, 3235–3244.
8. ISO 16112:2006, Compacted (Vermicular) Graphite Cast Irons—Classification. Available online: http://www.iso.org/iso/catalogue_detail.htm?csnumber=37724 (accessed on 27 May 2015).
9. Davis, J.R. *ASM Specialty Handbook—Cast Irons*; ASM International: Geauga County, OH, USA, 1996; pp. 430–432.
10. Cook, R.D. Detection of Influential Observations in Linear Regression. *Technometrics* **1977**, *19*, 15–18.
11. Yamada, N. Evaluation of Uncertainty in Thermal Expansivity Measurements. *Netsu Sokutei* **2002**, *29*, 72–81.
12. ISO/IEC Guide 98–3:2008, Uncertainty of Measurement—part 3: Guide to the Expression of Uncertainty in Measurement. Available online: http://www.iso.org/iso/catalogue_detail.htm?csnumber=50461 (accessed on 27 May 2015).
13. *Netzsch-Gerätebau-GmbH Expansion Tables for Dilatometer Standards*; Gerätebau GmbH: Selb, Germany, 1995.